ACS APPLIED MATERIALS & INTERFACES

Open Access

This article is licensed under CC-BY-NC-ND 4.0

www.acsami.org

Research Article

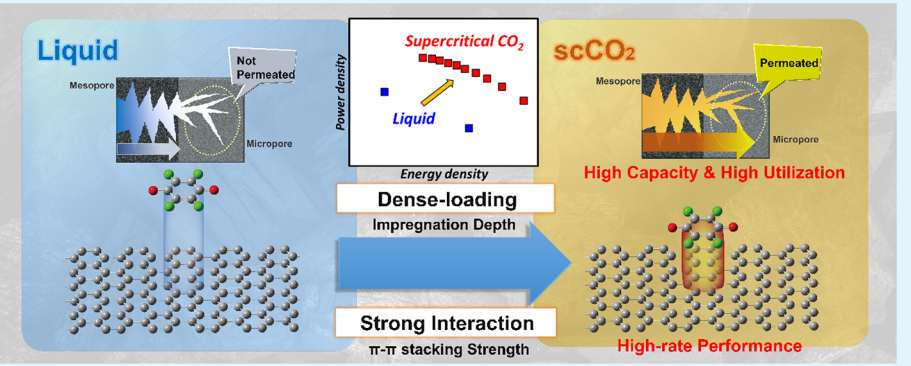
Supercritical CO_2-Induced Quinone Confinement and Interfacial Polarization in Microporous Carbon Electrodes for Aqueous All-Organic Batteries

Yuta Nakayasu,* Shu Sokabe, Naoka Nagamura, Chie Ooka, Tomoya Yamada, Kayoko Kobayashi, and Masaru Watanabe

Cite This: *ACS Appl. Mater. Interfaces* 2026, 18, 14947−14959

Read Online

ACCESS | Metrics & More | Article Recommendations | Supporting Information



ABSTRACT: Aqueous organic batteries provide a sustainable and metal-free alternative to conventional electrochemical storage, with performance often limited by modest active material loading and incomplete utilization inside porous carbon hosts. We report a simple all-organic full cell in which supercritical CO_2 ($scCO_2$) impregnation loads halogenated quinones into activated carbon (AC) and reorganizes the interface in a way that accelerates charge transfer. Using a minimal formulation, 1,5-dichloroanthraquinone is incorporated at approximately 38 wt % loading in the quinone/AC composite (prior to binder addition) with full electrochemical utilization, corresponding to high-density filling of the micropores rather than a high overall active-mass fraction, and serving as evidence of effective pore accessibility. Micropore analysis indicates about 90% of a micropore-limited upper bound. Small-angle X-ray scattering shows an increase in the high-q electron density correlation length, consistent with strengthened $\pi-\pi$ stacking and denser intrapore packing under supercritical conditions. We extracted interfacial electronic state information that can change with the impregnation route: comparative C K-edge X-ray absorption and X-ray photoelectron spectroscopy reveal core-level shifts consistent with a modified electronic environment and enhanced interfacial polarization in the $scCO_2$-impregnated samples relative to liquid-impregnated controls; confinement- and packing-related effects may also contribute. In aqueous full cells, the supercritical route gives a 60% increase in energy density and a clearly improved rate response relative to liquid-phase impregnation, while retaining 95% of the capacity after 1000 cycles; electrochemical impedance spectroscopy likewise shows a lower apparent charge transfer resistance for electrodes fabricated via supercritical impregnation, indicating faster interfacial kinetics. Taken together, these results demonstrate that $scCO_2$ impregnation promotes $\pi-\pi$-stacking-driven intrapore ordering and near-complete utilization in porous carbon quinone electrodes, translating nanoscale organization into device-level gains in a simple metal-free aqueous system.

KEYWORDS: *supercapacitors, energy, batteries, carbon, supercritical CO_2, quinones, organic battery, $\pi-\pi$ stacking*

1. INTRODUCTION

The accelerating deployment of intermittent renewables has placed higher demands on stationary electricity storage.[1] Current behind-the-meter installations depend mainly on lead−acid and lithium-ion batteries (LIBs),[2] which in turn rely on Co- and Ni-rich layered/spinel cathodes characterized by limited specific capacity,[3] nonrenewable graphite anodes,[4,5] and flammable organic-carbonate electrolytes. Even the latest advances—Fe-based polyanionic cathodes,[6,7] metal-free organic electrodes,[8,9] iron-catalyzed graphitization of sustainable carbons,[10−12] and nonflammable solid electrolytes[13]—cannot address the metals−cost−safety nexus.

Received: October 28, 2025
Revised: February 21, 2026
Accepted: February 25, 2026
Published: March 4, 2026



Downloaded via NATL INST FOR MATLS SCIENCE (NIMS) on July 17, 2026 at 09:32:03 (UTC).
See https://pubs.acs.org/sharingguidelines for options on how to legitimately share published articles.

© 2026 The Authors. Published by American Chemical Society

Aqueous systems inherently avoid the fire risk; however, the 1.23 V thermodynamic window of water restricts improvements in energy density. Water-in-salt electrolytes have recently pushed the practical limit to ≈ 3 V;[14] however, state-of-the-art Zn-ion batteries still fade because of Mn/V-oxide dissolution below ≈1.1 V[15] and the life-cycle burden of Zn production.[16] Aqueous supercapacitors deliver exceptional power but remain an order of magnitude lower in terms of energy density even with the latest 2.8 V zwitterionic electrolytes.[17−19] High-energy all-polymer aqueous batteries can reach gravimetric energies as high as 153 Wh kg^{-1}, facilitated by redox-active conductive polymers in fluorinated water-in-polymer electrolytes.[20] While promising, these systems face multiple hurdles for practical deployment: they rely on expensive and fluorinated salts (e.g., NaTFSI), involve multistep polymer synthesis and coating processes, and report energy densities calculated only from the active material mass.

In contrast, low-molecular-weight organic monomers, as electrode materials, offer a structurally simpler and synthetically scalable route, enabling high utilization, high redox-site density, solvent-free processing, and compatibility with sustainable carbon frameworks. All-organic monomer batteries overcome the aforementioned hurdles: discrete molecules provide well-defined two-electron redox centers, tolerate simple solution or dry impregnation, and allow rational design to suppress dissolution.[21−24] Tomai et al. paired tetrachloro-1,4-benzoquinone (TCBQ) with dichloroanthraquinone (DCAQ), achieving an operating voltage of ≈0.6 V per cell and excellent cycling.[25] Using Maxsorb, which is a petroleum-pitch-derived activated carbon (AC) with a Brunauer−Emmett−Teller (BET) surface area >3000 m^2 g^{-1} and abundant micropores,[26] we later achieved a specific energy of 14 Wh kg^{-1} and stacked the cells to ≈6 V without stability loss.[27,28]

A critical bottleneck in the use of organic monomers for batteries is monomer loading in porous carbons: liquid acetone impregnation saturates at ≈30 wt %[25,27] whereas gas-phase adsorption yields higher loadings, though the utilization is poor.[29,30] In microporous carbon electrodes, pushing the monomer fraction beyond ∼30 wt % can lead to dissolution/leaching and increased polarization unless the system is carefully engineered.[31,32] Accordingly, device-level performance metrics (energy, rate capability, cycling retention) are a more meaningful basis for comparison than simply maximizing the gravimetric loading. We note that with optimized molecular design and electrolyte conditions, higher active-mass fractions have been achieved without compromising stability in certain systems; however, those cases typically involve specially tailored hydrophobic molecules or confinement strategies that lie outside the scope of our work.[33,34]

Supercritical CO_2 ($scCO_2$) offers gas-like diffusivity and near-zero surface tension, enabling molecules to permeate deep into carbon micropores and to deposit uniformly upon depressurization without solvent residues. In practice, batch $scCO_2$ impregnation has commercial precedents in water-free textile dyeing and wood protection, demonstrating multihundred-liter throughput and closed-loop CO_2 recycle.[35,36] For activated carbons, $scCO_2$ impregnation typically yields a significant increase in monomer loading.[37,38] Although the method requires pressure-rated vessels (higher CAPEX), OPEX is partly offset by eliminating organic solvents and postdrying and by CO_2 recycle.[35,39] For electrodes, the same batch logic applies—powder-level impregnation upstream of slurry mixing or direct treatment of carbon cloth/paper—and scales via vessel size and parallel reactors. Remaining risks—process optimization and potential desorption/leaching—are mitigated by confining molecules in subnanometer micropores and by electrolyte choice. Representative $scCO_2$ impregnation studies in Li−S composites have likewise boosted loading and rate capability, although they emphasize performance and rarely probe interfacial conditions within carbon micropores.[40−43] These considerations motivate our use of $scCO_2$ in the present proof-of-concept study to maximize active-material loading and interfacial contact. Equally important, we seek to understand the mechanistic impact of this approach—specifically how $scCO_2$ impregnation alters the quinone−carbon interface. By probing the interfacial molecular packing (e.g., $\pi-\pi$ stacking) and electronic interactions, we can elucidate how such changes underpin the improved charge-transfer kinetics and utilization efficiency.

Despite the widespread use of X-ray absorption spectroscopy (XAFS) to probe metal-based electrodes, no study has yet correlated the nanoconfinement of wholly organic quinones with charge-transfer resistance at the electrode−electrolyte interface.[44−49] Here we directly observe—and mechanistically link—$scCO_2$-enabled strengthening of quinone−carbon $\pi-\pi$ stacking to reduced charge-transfer resistance ($R_{ct,app}$) and near-complete utilization, as supported by C K-edge XAFS and electrochemical evidence. Additionally, we employ X-ray photoelectron spectroscopy (XPS) to probe the electrode surface. The XPS analysis reveals shifts in the binding energies (BEs) of quinones indicative of stronger electronic interaction with the carbon, further corroborating that altered interfacial states (chemical bonding and electronic structure) are responsible for the enhanced performance.

To the best of our knowledge, our preliminary report on TCBQ derivatives remains the only published example of fabricating an organic-monomer electrode by supercritical-fluid impregnation.[50] Although that proof-of-concept achieved dense loadings in microporous carbons, the virtually nil solubility of nonpolar chloranil in neat $scCO_2$ limited reproducibility, left subnanometer micropores unfilled, and provided no insight into how confinement modifies monomer electronic structure. In contrast, the present study employs ethanol-entrained $scCO_2$ to impregnate a chlorinated quinone (DCAQ) with polarizable functional groups into micropores, enabling the first full-cell demonstration and spectroscopic analysis of confinement-induced interfacial effects. This knowledge gap makes it unclear how nanoconfinement affects the interfacial chemistry of quinones—for example, whether confinement induces closer $\pi-\pi$ stacking or changes in the electronic state—even though such interfacial state changes are likely critical for charge-transfer kinetics. Addressing this gap is essential for rationally improving device performance. Consequently, the field still lacks a general strategy that (i) drives quinones with polarizable functional groups such as DCAQ deep into micropores with full electrochemical access and (ii) correlates their molecular packing with charge-transfer kinetics. To resolve these issues, we devised a supercritical-fluid protocol that combines an ultralow (3.5 wt %) ethanol entrainer with the ultrahigh-surface-area carbon Maxsorb.

Here, we address both the loading bottleneck and the mechanistic knowledge gap by coupling an ultralow-entrainer supercritical CO_2 process with C−K edge XAFS. To this end we use $scCO_2$ containing only 3.5 wt % ethanol to impregnate DCAQ uniformly throughout the meso- and, crucially, subnanometer micropores of Maxsorb, achieving a record 38

https://doi.org/10.1021/acsami.5c21457
ACS Appl. Mater. Interfaces 2026, 18, 14947−14959

wt % loading with nearly complete electrochemical utilization—a result that reflects effective redox accessibility within the confined pore network. N_2/CO_2 sorption shows that $scCO_2$ accesses micropores left vacant by liquid methods, while C K-edge XAFS measurement reveals face-to-face $\pi-\pi$ stacking that halves the charge-transfer resistance. When the resulting DCAQ anode is paired with a supercritically loaded TCBQ cathode, the aqueous full cell delivers 22.3 Wh kg^{-1} at 0.1 A g^{-1}, based on the total electrode mass excluding binder. This corresponds to nearly 100% utilization of the ~38 wt % active material, with 54% capacity retention at 10 A g^{-1}, and 95% energy retention after 1000 cycles at 2 A g^{-1}. For the first time, we establish a pore-scale-to-device-level causality: $scCO_2$ organizes quinones into ordered $\pi-\pi$ stacks within micropores, reduces $R_{ct,app}$, and enables full electrochemical accessibility at practical loading levels, establishing a pore-scale link between $scCO_2$-driven intrapore ordering and reduced polarization in a proof-of-concept aqueous all-organic full cell. While $scCO_2$ processing is potentially scalable, the present work focuses on mechanistic interfacial and confinement effects rather than application-level optimization.

2. EXPERIMENTAL SECTION

Materials and Chemicals

AC (Maxsorb MSC-30) was purchased from Kansai Coke Chemicals Co., Ltd. DCAQ and TCBQ were purchased from Tokyo Chemical Industry Co., Ltd. PTFE (6-J) was purchased from Chemours-Mitsui Fluoroproducts Co. Ltd. (Tokyo, Japan).

Impregnation of DCAQ into AC Using $scCO_2$

As depicted in Figure 1(a), DCAQ was impregnated into Maxsorb using an entrainer. The critical temperature and pressure of CO_2 were

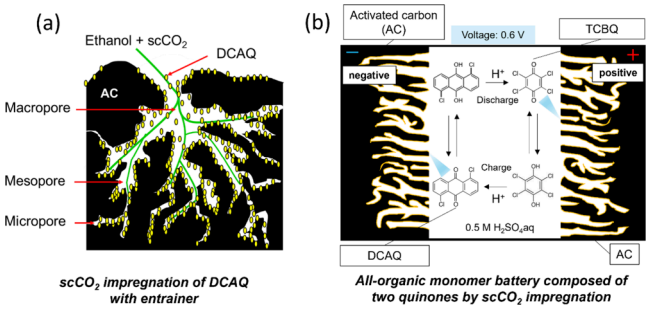


Figure 1. Schematics of (a) supercritical CO_2 impregnation of DCAQ with ethanol as entrainer; (b) aqueous all-organic monomer battery.

31.1 °C and 7.38 MPa, respectively. $ScCO_2$ impregnation of DCAQ was performed using the equipment described in a previous report.[50] DCAQ (1.0 g) and AC (0.1 g) were loaded into a SUS316 stainless steel tube reactor (volume 5.71 mL). The AC sample was placed in a small container made of copper plates (to prevent spillage or direct mixing with the quinone). The reactor was then placed in a vat filled with aluminum balls on a hot plate, which was heated to the desired temperature (75–155 °C depending on the run). Liquid CO_2 was introduced using a high-pressure pump (Jasco PU-2080-CO2 Plus) and brought to the set pressure (15–25 MPa). After reaching the target pressure, the system was equilibrated for 10 min and then isolated by closing the inlet valve. The sealed reactor was kept at the set temperature and pressure for 24 h to allow DCAQ to dissolve and diffuse into the AC pores. After this 24 h supercritical soaking period, the reactor was depressurized by rapidly venting the CO_2 to ambient pressure (by opening the outlet valve). The reactor was then opened, and the impregnated AC sample was removed from the copper container. No post-treatment (such as rinsing or washing) was performed on the sample. As a result, the final quinone loading in the AC was lower than the initial 10:1 mass ratio.

Liquid impregnation of quinones into AC was used as the control. First, DCAQ (300 mg) was dissolved in acetone (100 mL) and sonicated for 10 min. AC (700 mg) was then dispersed in the solution and sonicated for 1 h. The solution was stirred at 60 °C to facilitate the evaporation of the acetone, and DCAQ was impregnated into the pores of the AC.

Table 1 summarizes the $scCO_2$ impregnation conditions. Impregnated samples were denoted based on the temperature–pressure–time

Table 1. Conditions of $scCO_2$ impregnation of DCAQ into AC

sample	pressure [MPa]	temperature [°C]	time [h]	entrainer
AC_L				
$AC_{75_25_24}$	25	75	24	
$AC_{105_15_24}$	15	105	24	
$AC_{155_25_24}$	25	155	24	
$AC_{155_25_72}$	25	155	72	
$AC_{155_25_144}$	25	155	144	
$AC_{155_25_24_E}$	25	155	24	3.5 wt % EtOH

(T_P_t, respectively) combinations. For example, $AC_{T_P_t}$ and AC_L represent samples formed by $scCO_2$ impregnation and liquid impregnation, respectively. The presence of the entrainer is marked with an "E" next to the notation, such as $AC_{T_P_t_E}$.

Electrochemical Measurement of DCAQ Half-Cell Setup

AC impregnated with DCAQ was mixed with a PTFE binder at a weight ratio of 9:1. The mixture (5 mg) was pressed to form pellets (diameter, φ = 5.5 mm) at a mass loading of 21.05 mg cm^{-2}. An aqueous solution of H_2SO_4 (0.5 M), whose concentration was chosen based on prior optimization reported in the literature,[28] bubbled with nitrogen for 2 h was used as the electrolyte. The electrodes immersed in the electrolyte were placed under vacuum for 30 min to remove the bubbles. A three-electrode cell was then assembled, comprising DCAQ-impregnated AC as the working electrode, an AC electrode (AC and PTFE at a weight ratio of 9:1) (which is more than five times heavier than the working electrode) as the counter electrode, aqueous H_2SO_4 solution (0.5 M; 70 mL) as the electrolyte, and an Ag/AgCl electrode as the reference electrode. Electrochemical measurements were conducted using a potentiostat/galvanostat (Solartron Analytical) under ambient conditions. The capacity, cycle performance, and rate performance were evaluated through galvanostatic charge–discharge tests at 0.1–10 A g_{AC+imp}^{-1} in the voltage range of −0.4–0.5 V. For the half-cell performance, the current density calculations were based on the weight of the entire electrode excluding the binder weight. All specific capacities (mAh g^{-1}) reported in this work are normalized to the total mass of the quinone/activated-carbon composite (excluding the binder), unless otherwise noted.

Electrochemical Measurement of the Full-Cell

As illustrated in Figure 1(b), a full cell was assembled employing TCBQ as the cathode and DCAQ as the anode. TCBQ was impregnated under supercritical conditions (105 °C, 15 MPa, and 24 h), which were the optimal electrode performance conditions established in our previous work.[50] PTFE was mixed as a binder with $AC_{TCBQ_105_15_24}$ and $AC_{155_25_24_E}$ at a ratio of 9:1 in a mortar to prepare cathode and anode pastes. The TCBQ cathode paste was spread thinly at a mass loading of 20.20 mg cm^{-2}, pressed onto a gold mesh with a diameter of 5.5 mm, hollowed out, and welded with a gold wire. The DCAQ electrode was fabricated by spreading the paste thinly at a mass loading of 5.05 mg cm^{-2}, crimping it onto a gold mesh with a diameter of 11 mm, welding a hollowed-out Au wire to it using a press machine, and lightly tapping it with a hammer to ensure a sufficient crimp. The difference in thickness between the TCBQ and DCAQ electrodes despite having the same weight can be attributed to the significant increase in the resistance of the DCAQ electrode with increasing thickness, which in turn can be

https://doi.org/10.1021/acsami.5c21457
ACS Appl. Mater. Interfaces 2026, 18, 14947–14959

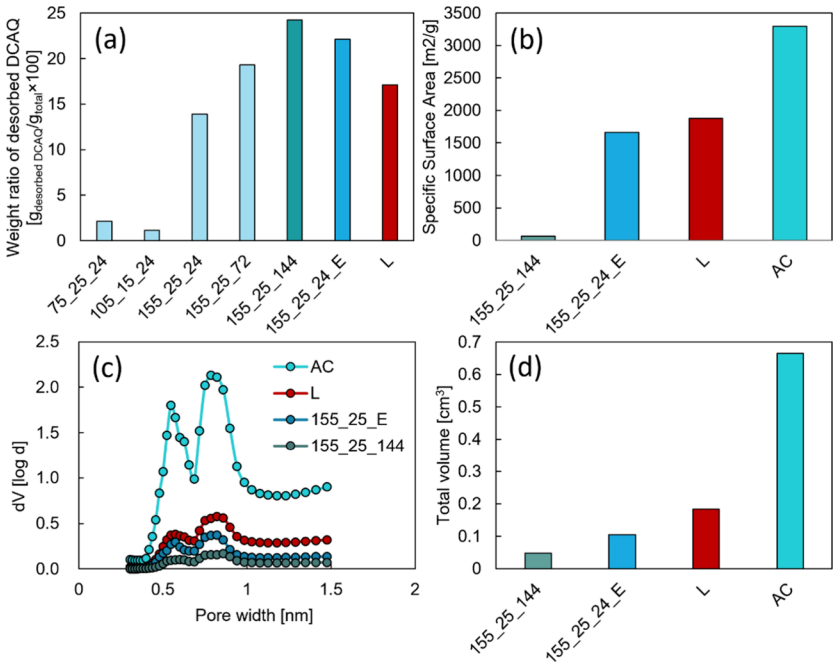


Figure 2. (a) Weight ratio of the desorbed DCAQ calculated from the TG results. (b) Specific surface area calculated using the BET method. (c) Micropore size distribution calculated using the NLDFT and CO_2 adsorption/desorption methods. (d) Total pore volume in the DCAQ-impregnated AC with the pore diameter of less than 1 nm.

attributed to its susceptibility for proton diffusion inhibition caused by the increased thickness. Measurements were performed in a 0.5 M H_2SO_4 aqueous solution with nitrogen bubbling using an electrochemical measurement device (SI 1280−2, Toyo Technica, Inc.). The energy density was calculated by dividing the filled area in two, as shown in Figure S1, at constant current rates of 0.26, 0.28, and 2.6 A g_{AC+imp}^{-1} and in the voltage range of 0−1 V. The data for the fifth cycle were extracted. For the rate characteristics, constant-current measurements were demonstrated in the voltage range 0−1.2 V and current rate range of 0.1−10 A g_{AC+imp}^{-1}, and the data for the second cycle were extracted. For cyclic characteristics, constant-current measurements were performed over 1000 cycles in the range of 0−1.2 V at 2 A g_{AC+imp}^{-1}. The results for the first and 1000th cycles were compared. For the full-cell performance, the current density, power density, and energy density calculations were based on the total weight of the cathode and anode electrodes, excluding the binder weight. In contrast, the Ragone-plot energy and power densities (Figure 4(f)) are reported on a total-electrode-mass basis including the binder, in order to enable a fair comparison with literature data.

Material Characterization

The specific surface area (SSA) was measured using an N_2 adsorption/desorption analyzer (Bellsorp Mini II) and calculated from the adsorption points for the relative pressure range of 0.1−0.25 P/P_0 using the BET theory. The pore distribution was measured using a pore size analyzer (QUADRASORB evo, Quantachrome Instruments) and calculated using the nonlocalized density functional theory (NLDFT). To quantify how closely the measured loading approaches the capacity set by the host's micropores, we evaluated a micropore-limited upper bound and corresponding filling fractions.[51,52] The detailed analysis method is described in SI (eqs S1−S4). Thermogravimetric (TG) measurements were performed using a TG/DTA 6200 instrument (EXSTAR 6000 series; Seiko Instruments Inc., Japan). The temperature was increased from 30 to 110 °C at a rate of 10 °C min^{-1} under an N_2 flow of 200 mL min^{-1}. The temperature was maintained for 20 min, increased again to 400 °C (10 °C min^{-1}), and then kept constant for 40 min. From the TG results, the weight ratio of the desorbed DCAQ was calculated using the following:

$$\text{DCAQ ratio [\%]} = \frac{TG_{total} - TG_{400}}{TG_{total}} \times 100 \quad (1)$$

The amount of Cl in the sample was determined through combustion ion chromatography (CIC) analysis, which was outsourced to Shimadzu Techno Research Corporation. The loading amount of DCAQ and TCBQ in the AC was determined from the Cl content measured by CIC. After liquid-phase and $scCO_2$ impregnations, small-angle X-ray scattering (SAXS) measurements and Guinier-type analysis used to estimate micropore-regime correlation lengths are described in SI (eq S5). The procedure follows the unified Guinier/power-law framework and standard data-reduction practice.[53−55]

XAFS measurements of the C K-edge were conducted at BL-13B of the High Energy Accelerator Research Organization (KEK) in Ibaraki, Japan, X-ray diffraction (XRD) using Cu−Kα radiation was conducted with an Ultima IV (RIGAKU, Japan) and X-ray photoelectron spectroscopy (XPS) measurements were performed using a PHI 5000 VersaProbe II. Cyclic voltammetry (CV) measurements of TCBQ were performed at five scan rates ranging from 1.0 to 10 mV s^{-1} within a potential window of 0−1 V versus the Ag/AgCl electrode. Electrochemical impedance spectroscopy (EIS) was conducted at frequencies ranging from 0.1 Hz to 20 kHz with an amplitude of 10 mV. The Nyquist plots were analyzed in ZView using the built-in semicircle (depressed-arc) estimation. The apparent charge-transfer resistance ($R_{ct,app}$) was quantified as the width of the high-frequency semicircle (difference between the low- and high-frequency real-axis intercepts). The degree of arc depression was described by the CPE exponent α estimated from the depression angle. When required, the CPE coefficient (Y_0) was estimated from ω_{max}, $R_{ct,app}$, and α (see Supporting Information).

3. RESULTS AND DISCUSSION

3.1. $ScCO_2$ Impregnation of DCAQ with Entrainer

Figure 2a shows the weight ratio of desorbed DCAQ during the TG measurement. Clearly, a small amount of DCAQ was loaded into $AC_{75_25_24}$ and $AC_{105_15_24}$ under the aforementioned conditions. According to a previous report, the liquid impregnation process showed a loading rate of approximately

https://doi.org/10.1021/acsami.5c21457
ACS Appl. Mater. Interfaces 2026, 18, 14947−14959

30% for TCBQ, whereas the loading rate calculated by TG was approximately 17%.[50] Accordingly, the TG measurement for DCAQ is likewise expected to underestimate the actual loading, just as it does for TCBQ. In fact, a loading of 17 wt % was obtained in AC_L. This indicates that the organic molecules were not fully volatilized once they were loaded into the micropores. Under the conditions of $AC_{155_25_24}$, a loading result of approximately 14 wt % was obtained. As the $scCO_2$ impregnation time was increased to 72 and 144 h, the relative loading amounts increased to 19 and 24 wt %, respectively. This can be ascribed to the enhancement in solute−solvent interactions due to the increase in temperature and pressure,[56] thereby increasing the DCAQ concentration. In contrast, when ethanol was used as the entrainer, a higher relative loading of 22 wt % was observed compared with $AC_{155_25_72}$ and AC_L. Compared with AC_L, a 1.3-fold increase for $AC_{155_25_24_E}$ and 1.4-fold increase for $AC_{155_25_144}$ in loading were achieved. Therefore, the addition of ethanol as an entrainer was effective for DCAQ with polarizable functional groups.

Figure 2b shows the measurement results of the BET-based SSA under liquid impregnation conditions, highlighting the higher loading amounts of $AC_{155_25_144}$ and $AC_{155_25_24_E}$. The SSA decreased as the DCAQ impregnation loading increased. This suggests that the pore volume and SSA decreased as DCAQ was loaded onto the AC. In $AC_{155_25_144}$, the SSA significantly decreased compared with that in AC_L, indicating that the pores may have been filled due to the multiple depositions of DCAQ. In contrast, for $AC_{155_25_24_E}$, despite the increase in the impregnation loading, the decrease in the SSA was relatively small. This suggests that the pores were likely impregnated with DCAQ without completely filling them.

Figure 2c shows a detailed measurement of the micropore distribution obtained from the CO_2 adsorption−desorption measurements. For the micropores, the two samples impregnated with $scCO_2$ exhibited a significant decrease compared with AC_L, indicating that a large portion of the increased impregnation loading of DCAQ was adsorbed onto the micropores. Similar to TCBQ impregnation in a previous study,[50] this can be ascribed to $scCO_2$, which transports DCAQ to the micropore depth at high concentrations owing to its high diffusivity and solubility.

Figure 2d shows the total pore volume. The total pore volume with a pore diameter of 1 nm or less was lower after $scCO_2$ impregnation than that after liquid impregnation, with $AC_{155_25_144}$ exhibiting the smallest pore volume. Based on these results, similar to TCBQ, $scCO_2$ impregnation was superior to liquid impregnation in terms of impregnation into smaller pores.

These results confirm that $scCO_2$ impregnation is more effective than liquid-phase impregnation for loading DCAQ into subnanometer pores, consistent with previous observations for TCBQ.[50] To quantify the degree of pore filling, we quantified the DCAQ loading for AC_L and $AC_{155_25_24_E}$ by CIC, which provides an accurate, absolute measurement for the φ calculations (Table 2). Using the micropore volume V_{micro} (0.3−1.5 nm) ≈ 0.663 $cm^3\ g^{-1}$ and assuming a confined-phase density $\rho_{conf} \approx 1.1\ g\ cm^{-3}$, we estimated a theoretical maximum loading of $w_{max} = 0.42$. Other calculated parameters were shown in Table S1. The choice of ρ_{conf} is based on the well-known Gurvich rule that an adsorbate in saturated micropores approaches its liquid density and on typical liquid densities of chlorobenzene (1.1 g cm^{-3}). The measured DCAQ content in the $AC_{155_25_24_E}$ (w = 0.38) corresponds to ∼90% of the micropore-limited upper bound ($w/w_{max} \approx 0.90$), whereas AC_L reaches only $w/w_{max} \approx 0.64$.

Table 2. Impregnation Loading of DCAQ Estimated by CIC Measurement

samples	Cl [wt %]	DCAQ [wt %]	w/w_{max} [-]
AC_L	6.9	27	0.64
$AC_{155_25_24_E}$	9.6	38	0.90

To investigate micropore-scale structural ordering, we obtained SAXS profile shown in Figure S2 and a Guinier-type fit to the high-q SAXS window (1.72−3.89 nm^{-1}),[53,54] following the Unified Guinier−Porod approach for the smallest-length-scale level; the fitted r_g was converted to a real-space electron-density correlation length 2 r_g.[55] As summarized in Table 3, this correlation length increases from 0.963 nm for the liquid-impregnated DCAQ to 1.056 nm for the $scCO_2$-impregnated DCAQ (+9.7%), consistent with enhanced intrapore ordering under $scCO_2$ conditions.[57,58] We note that these SAXS-derived values represent electron-density correlation lengths rather than gas-sorption pore diameters; absolute placement relative to pristine AC can vary with contrast and filling,[57,59] while the liquid < $scCO_2$ trend is robust across quinones.

Table 3. Micropore-Regime Correlation Length from SAXS (Guinier-Type Fit)

sample	q-window (nm^{-1})	r (nm)	d (=2r, nm)
AC (Maxsorb)	1.72−3.89	0.743	1.487
AC_L	1.72−3.89	0.963	1.926
$AC_{155_25_24_E}$	1.72−3.89	1.056	2.112

3.2. Electrochemical Measurements of DCAQ Half Cells

Figure 3(a) shows the specific charge capacity in the voltage range of −0.4−0.5 V at 1 A g_{AC+imp}^{-1} for $AC_{155_25_144}$, $AC_{155_25_24_E}$, and AC_L, where g_{AC+imp} represents the weight of the entire electrode excluding the binder weight. The charge capacities under the other conditions are provided as Figure S3.

$AC_{155_25_144}$ (65.7 mAh g_{AC+imp}^{-1}) and $AC_{155_25_24_E}$ (92.5 mAh g_{AC+imp}^{-1}) exhibited higher capacities than AC_L (41.9 mAh g_{AC+imp}^{-1}) and a previously reported value of 51 mAh g_{AC+imp}^{-1} at a rate of 0.26 A g_{AC+imp}^{-1}.[25] $AC_{155_25_24_E}$ demonstrated the highest specific charge capacity, which was 1.8 times greater than that of AC_L. However, in $AC_{155_25_144}$, which had a higher impregnation loading than that of $AC_{155_25_24_E}$, the specific charge capacity was slightly lower than that of $AC_{155_25_24_E}$.

To further analyze this, Figure 3(b) shows the charge/discharge curves at 1 A g_{AC+imp}^{-1} for $AC_{155_25_24_E}$, $AC_{155_25_144}$, and AC_L. The results reveal that $AC_{155_25_24_E}$, which had the highest specific charge capacity, has a plateau position near −0.07 V, indicating the lower overpotential due to redox reactions. From the cyclic voltammetry results, $AC_{155_25_24_E}$ likewise exhibited a smaller overpotential than AC_L; both showed a value of −0.07 V (Figure S4). Conversely, $AC_{155_25_144}$ and AC_L exhibited significantly higher overpotentials. This suggests that the increased $scCO_2$ impregnation time in $AC_{155_25_144}$ resulted in the stacking of multiple layers of DCAQ, which increased the interfacial resistance. However, for AC_L, the uneven distribution of the solute could be ascribed to the remaining solvent on the surface during drying, which could have increased the interfacial resistance and overpotential. As an additional practical benchmark, a DCAQ/AC/PTFE electrode

https://doi.org/10.1021/acsami.5c21457
ACS Appl. Mater. Interfaces 2026, 18, 14947−14959

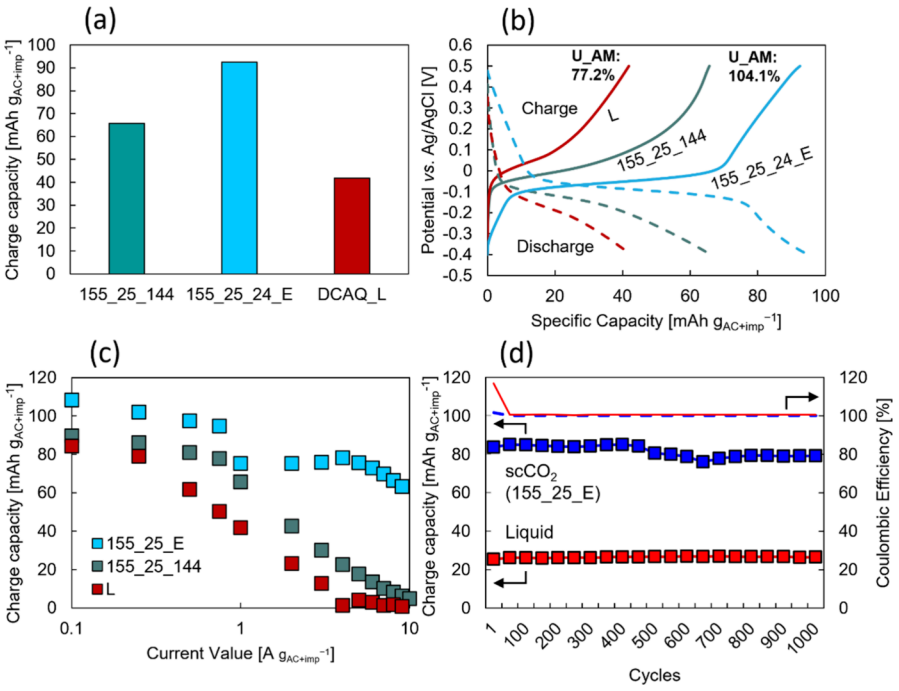


Figure 3. (a) Specific charge capacity measured at 1 A g_{AC+imp}^{-1} in the potential range of −0.4−0.5 V, (b) charge−discharge curve at 1 A g_{AC+imp}^{-1} in the potential range of −0.4−0.5 V and utilization efficiency (U_AM) and (c) Rate characteristics measured in the potential range of −0.4−0.5 V for $AC_{155_25_24_E}$, $AC_{155_25_144}$, and AC_L. (d) Cycle characteristics for two samples (liquid impregnation and $scCO_2$ impregnation at 155 °C and 25 MPa with ethanol) measured in the potential range of −0.4−0.5 V at 1 A g_{AC+imp}^{-1}.

was prepared by simple physical mixing (1 h ball milling) at the same nominal DCAQ fraction as $AC_{155_25_24_E}$. When the electrochemical test was initiated from the reduction process, this ball-milled electrode exhibited almost no accessible capacity under the same conditions (Figure S5). This result indicates that simple physical mixing does not readily generate an electrochemically addressable redox state of DCAQ, in contrast to the $scCO_2$-impregnated electrode. For $AC_{155_25_24_E}$, the faster removal of the solvent in the $scCO_2$ process compared with liquid impregnation and enhanced adsorption through the $\pi-\pi$ interactions helped maintain the adsorbed state of DCAQ, which exhibited the most stable interaction with the AC pore surface. Supercritical CO_2 has a lower density than the acetone used in the liquid impregnation process, resulting in a lower distribution coefficient of DCAQ to the solvent and a relatively stronger interaction with AC. This phenomenon is also observed in high-performance liquid chromatography (HPLC) and supercritical fluid chromatography (SFC). Indeed, pyrenylethyl and pentabromophenyl stationary phases show stronger $\pi-\pi$ interactions in SFC than in HPLC.[60]

Figure 3c shows the rate performance of $AC_{155_25_24_E}$, $AC_{155_25_144}$, and AC_L. $AC_{155_25_24_E}$ and $AC_{155_25_144}$ exhibited better rate properties than AC_L. Moreover, $AC_{155_25_24_E}$ exhibited higher charge−discharge capacities than $AC_{155_25_144}$ and AC_L at all current values, with a lower rate of capacity decrease even at currents above 2 A g_{AC+imp}^{-1}. This can be attributed to the lower overpotential observed for $AC_{155_25_24_E}$ compared with the other two samples. Although $AC_{155_25_144}$ maintained a high specific charge capacity of up to 1 A g_{AC+imp}^{-1}, the specific charge capacity significantly decreased at currents above 1 A g_{AC+imp}^{-1} due to the increased interfacial resistance caused by the multilayer stacking of DCAQ.

Table 4 presents the theoretical and actual capacity, and the utilization efficiency of DCAQ in terms of the specific capacity.

Table 4. Theoretical and Actual Capacity, and Its Capacity Utilization (U_AM) in the Samples

samples	theoretical capacity [mAh g^{-1}]	actual redox capacity [mAh g^{-1}]	U_AM [%]
AC_L	52.0	40.2	77.2
$AC_{155_25_24_E}$	72.4	73.7	104.1

The redox capacity, excluding the electric double-layer capacitance (EDLC), was calculated using a previously reported method.[28] The redox capacity of TCBQ was also investigated using the same method (Supporting Information). The utilization efficiency of $AC_{155_25_24_E}$ exceeded 100% because of the redox capacity of the AC surface. This effect became more pronounced with increasing overpotential, indicating that the actual utilization efficiency of AC_L at 1 A g_{AC+imp}^{-1} was estimated to be less than 77.2%. Meanwhile, $AC_{155_25_24_E}$ exhibited a utilization efficiency of almost 100%, suggesting that the $scCO_2$ impregnation of DCAQ was almost fully utilized. This high utilization rate indicates the uniformity of the supercritical impregnation support. Figure S6a−c shows the rate properties of $AC_{155_25_24_E}$, $AC_{155_25_144}$, and AC_L at three specific currents. Evidently, $AC_{155_25_24_E}$ exhibited a lower overpotential and a higher amount of supported DCAQ, resulting in its higher specific capacities at all specific currents. Furthermore, the difference in the specific capacities owing to the overpotential increased with increasing specific current.

Figure 3d compares the cycling performance of the $AC_{155_25_24_E}$ and AC_L. $AC_{155_25_24_E}$ samples exhibit cyclic properties with the highest performance and could maintain 95% of their initial capacity after 1000 cycles, indicating their excellent cycle stability even with a loading of 38 wt % through scCO2 impregnation. In all the cycles, the Coulombic efficiency (CE) exceeded 100%. This can be attributed to the stronger adsorption of DCAQ supported on the AC surface through $\pi-\pi$

https://doi.org/10.1021/acsami.5c21457
ACS Appl. Mater. Interfaces 2026, 18, 14947−14959

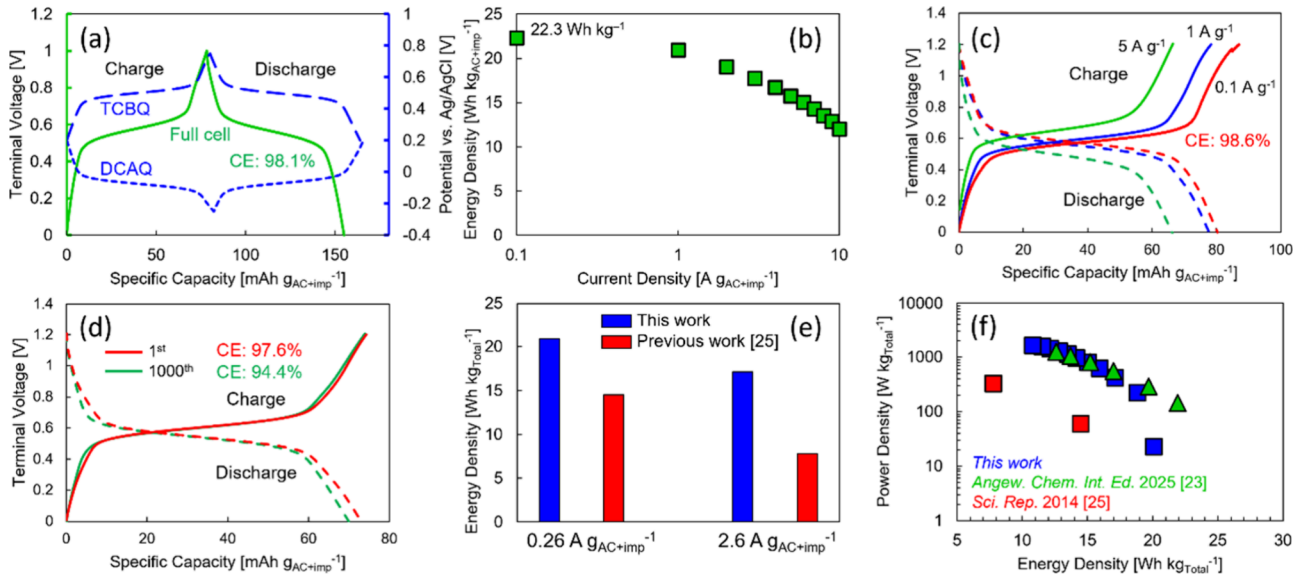


Figure 4. (a) Charge−discharge curves of the TCBQ cathode alone, DCAQ anode alone, and the full cell at 0.28 A g_{AC+imp}^{-1}. (b) Rate characteristics of the full cell. (c) Charge−discharge curves at varying specific currents. (d) Comparison of the energy density at the first and 1000th cycle. (e) Comparison of the energy density with previously reported data. (f) Ragone plot of full cells in this study with literature benchmarks.[23,25] The benchmark D-HATN//HSA data are taken from Table S10 of ref 23. All values are normalized to the total mass of electrode materials (active materials + conductive additives + binders). Note that ref 23 uses a higher active-material fraction (≈60 wt %) than this work (≈34 wt %).

interactions, which is more effective than the liquid impregnation process, similar to TCBQ (see Table S2). Notably, the reduction (discharge) process does not exhibit a pronounced rate limitation compared to oxidation, suggesting that the pore-confined architecture effectively minimizes kinetic asymmetry between the two redox states.

3.3. Electrochemical Measurements of a TCBQ−DCAQ Full Cell

TCBQ was impregnated under supercritical conditions at 105 °C, 15 MPa, and 24 h, which were the optimal electrode performance conditions established in our previous report.[50] The full-cell performance was evaluated using the TCBQ-impregnated AC as the cathode and the $AC_{155_25_24_E}$ as the anode.

Figure 4a shows the redox curves of the positive (TCBQ) and negative (DCAQ) electrodes as well as the charge−discharge curves of the full cell at 0.28 A g_{AC+imp}^{-1}. A plateau at around 0.6 V originates from the redox processes of both electrodes, including overpotential effects. The energy density reached 20.85 Wh kg_{AC+imp}^{-1}, which is comparable to that of the lead-acid batteries. However, the length of the plateau was longer when measured separately for the positive and negative electrodes, indicating that not all the impregnated DCAQ was utilized in the charge−discharge process. The CE at this time was 98.1%.

Figure 4b shows the change in the energy density in the range of 0.1−10 A g_{AC+imp}^{-1}. The energy density reached 22.3 Wh kg_{AC+imp}^{-1} at 0.1 A g_{AC+imp}^{-1}. The decrease in the energy density with the increasing rate remained low, demonstrating that both the positive and negative electrodes maintained a high rate performance in the full cell. Further, this indicates that the full cell could be charged to 80% of its capacity in 2 min. Figure 4c shows the charge−discharge curves at 0.1, 1, and 5 A g_{AC+imp}^{-1}. The energy density decreased with increasing rate value. In the voltage range of 0−1 V, the CE was 98.6% at 0.1 A g_{AC+imp}^{-1}. This CE value is higher than that of a previously reported all-organic battery.[61]

Figure 4d presents a comparison of the charge−discharge curves and energy density with the first and 1000th cycles at 2 A g_{AC+imp}^{-1}. No significant differences were observed in the potential difference of the plateau, which represents the redox reaction of quinones and the plateau length. This suggests that a small portion of the quinones is dissolved in the electrolyte because the incomplete utilization of infiltrated quinones has minimal effect on the charge−discharge process. Therefore, the capacity degradation was mainly attributed to the deterioration in the EDL capacity. At this point, the energy density was 19.0 Wh kg_{AC+imp}^{-1} in the first cycle and 18.1 Wh kg_{AC+imp}^{-1} in the 1000th cycle, retaining 95% of its initial energy density. After 1000 cycles, the CE decreased by approximately 3.3%.

Figure 4e presents the energy density at 0.26 and 2.6 A g_{AC+imp}^{-1}, compared with the previously reported energy density of a full cell with TCBQ and DCAQ impregnation into AC using the liquid impregnation method.[23] The full cell exhibited a 1.44 times higher energy density at 0.26 A g_{AC+imp}^{-1} and 2.20 times higher energy density at 2.6 A g_{AC+imp}^{-1}. This indicates a significant improvement in the performance of the full cell in the present battery, in which quinones were infiltrated into the AC using the $scCO_2$ impregnation process. This improvement can be attributed to the increase in the TCBQ/DCAQ loading and an improvement in the adsorption mode, which helped reduce the interfacial resistance and overpotential. The power density was calculated from the obtained rate capability. The Ragone plot in Figure 4f shows data from three sources: (i) our previous liquid-impregnation cells, (ii) the supercritical-loaded full cell, and (iii) a recent benchmark aqueous all-organic battery (ref. 23; values from Table S10). For an equitable device-level comparison, all energy and power densities in Figure 4f are normalized to the total mass of both electrodes including active materials, conductive additives, and binders, consistent with the normalization used in ref. 23. We note that the benchmark electrodes employ a higher active-material fraction (≈60 wt %) than our electrodes (≈34 wt %). In addition, the benchmark system is based on an engineered π-bridged 2D redox polymer

https://doi.org/10.1021/acsami.5c21457
ACS Appl. Mater. Interfaces 2026, 18, 14947−14959

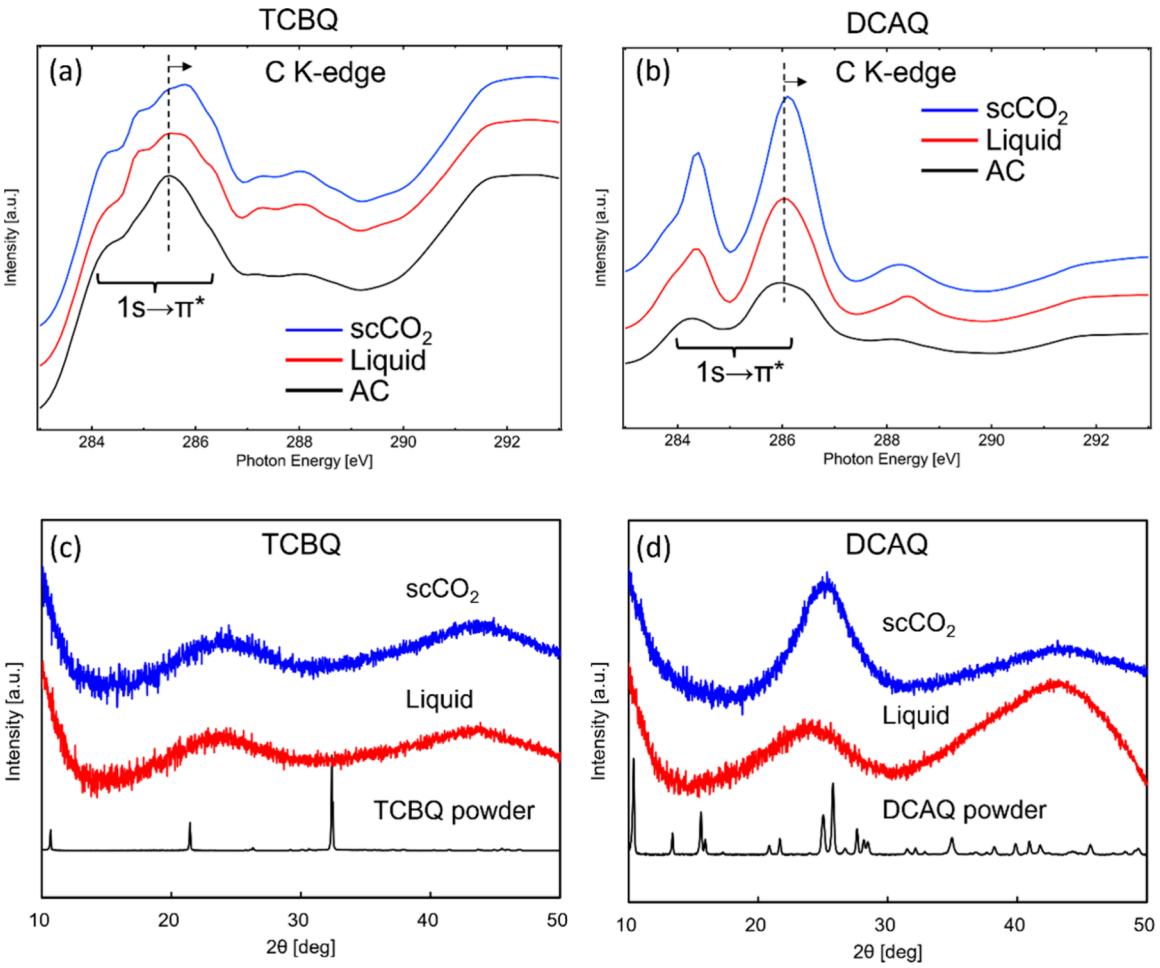


Figure 5. C K-edge XAFS spectra of (a) TCBQ-impregnated samples and (b) DCAQ-impregnated samples; XRD measurement results of (c) TCBQ-impregnated samples and (d) DCAQ-impregnated samples.

anode (D-HATN), whereas our full cell relies on physically confined small-molecule quinones in porous carbon enabled by a simple $scCO_2$ impregnation process. Under these conditions, our $scCO_2$-loaded full cell shows competitive performance and notably maintains higher energy output at high power, while remaining slightly lower at the lowest current densities. Nevertheless, our sample combines excellent cycling stability with a straightforward processing route, providing practical proof-of-concept for $scCO_2$-enabled intrapore ordering in a metal-free aqueous system. These device-level metrics are comparable to legacy aqueous systems on a total-electrode-mass basis, while highlighting improved rate response relative to the liquid-impregnated control.

To investigate the factors contributing to this high-rate performance, further structural characterization was conducted on both electrodes. $scCO_2$ refers to the $scCO_2$ impregnation conditions for each quinone in the full cell described above, while liquid denotes the liquid impregnation conditions using acetone. XAFS measurements were conducted to investigate the electronic state of C K-edge in TCBQ and DCAQ. As shown in Figure 5a,b, distinct differences can be observed between the liquid-phase and $scCO_2$ impregnations in the C K-edge XAFS spectra. In particular, the C 1s → π^* transition shifted to the higher energy side more prominently in the case of $scCO_2$ impregnation, suggesting a greater reduction in the π-electron density. This indicates that $scCO_2$ impregnation enhances $\pi-\pi$ stacking interactions, leading to a more compact molecular arrangement.

As shown in Figure 5c,d, the XRD patterns of pure TCBQ and DCAQ exhibit distinct diffraction peaks, confirming their original crystalline nature. However, after both liquid-phase and $scCO_2$ impregnations, the XRD patterns have broad peaks, indicating the absence of crystallinity in both cases. This suggests that in both the methods, TCBQ and DCAQ molecules were supported on AC without retaining their original ordered structures.[28,29] In general, when organic redox-active molecules become highly crystalline, their electronic conductivity decreases because the π-conjugated domains are separated by intermolecular packing gaps, which hinder efficient charge transfer. In contrast, in porous-carbon−supported systems, a less-crystalline or amorphous dispersion allows closer $\pi-\pi$ contact with the conductive carbon surface, facilitating electron exchange and lowering the interfacial resistance. Therefore, the strengthened $\pi-\pi$ interactions between the quinones and AC likely helped improve the rate performance by reducing resistance.

3.4. Exploration of Rate Capability Enhancement through Further Structural Characterization of TCBQ-Impregnated Activated Carbon

To further investigate the phenomena occurring during the $scCO_2$ impregnation process of quinones, a more detailed

https://doi.org/10.1021/acsami.5c21457
ACS Appl. Mater. Interfaces 2026, 18, 14947−14959

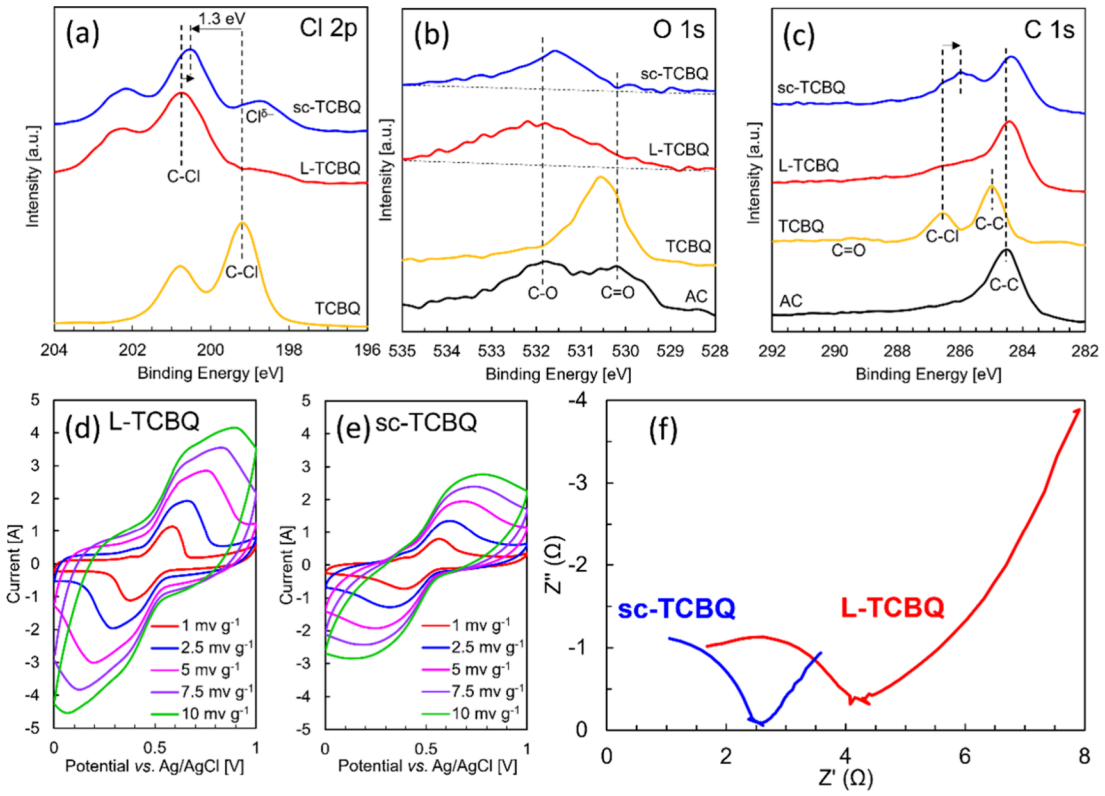


Figure 6. (a) XPS Cl 2p spectra deconvoluted into organochloride (C−Cl) and inorganic chloride: only the C−Cl doublet shifts to higher BE after $scCO_2$ impregnation; the inorganic chloride doublet remains fixed, excluding charging-induced rigid shifts. (b) XPS O 1s spectra. (c) XPS C 1s spectra. (d, e) Cyclic voltammetry (CV) curves at varying scan rates for L-TCBQ and sc-TCBQ. (f) Nyquist plots from electrochemical impedance spectra of L-TCBQ and sc-TCBQ.

structural and electrochemical characterization was conducted using TCBQ as a model system (Figure 6a−f).

Figure 6a shows the XPS Cl 2p spectra of TCBQ, TCBQ impregnated into AC via liquid impregnation (hereinafter, L-TCBQ), and TCBQ impregnated into AC via supercritical CO_2 impregnation (hereinafter, sc-TCBQ). Pure crystalline TCBQ exhibits a high degree of crystallinity (distinct XRD peaks, Figure 5c), and due to strong intermolecular $\pi-\pi$ stacking and charge-transfer effects within its crystal, its chlorine atoms show Cl $2p_{3/2}$ and Cl $2p_{1/2}$ core-level peaks at 199.2 and 200.8 eV, respectively—these are relatively low BEs for an organic compound, reflecting increased ionic character in the C−Cl bonds. In both impregnated samples, the main Cl 2p peaks appear at significantly higher BE (by more than 1.3 eV) compared to those of pure TCBQ, indicating that supporting TCBQ on AC modifies the electronic environment of the C−Cl moieties, consistent with an interfacial dipole and/or increased C−Cl bond polarization relative to crystalline TCBQ. We emphasize that XPS alone does not uniquely identify the microscopic origin of the shift, especially under high loading and confinement. Deconvolution of the Cl 2p spectra further shows that the organochloride (C−Cl) peak is shifted by ∼0.4 eV to higher BE in sc-TCBQ (relative to its position in L-TCBQ), while the inorganic chloride reference peak remains near 198−199 eV.[62] The higher BE of the Cl 2p component in sc-TCBQ (relative to L-TCBQ) is consistent with stronger interfacial polarization (and/or altered screening) under $scCO_2$ impregnation, without assigning a specific partial charge state to chlorine from XPS alone. Additionally, a small signal corresponding to ionized chloride (Cl^- at ∼198.8 eV) is detected and this minor component reflects ionic stabilization at the interface (e.g., interactions with electron-donating surface groups such as carbonyls) but does not alter the dominance of the higher-BE organochloride signal in the sc-TCBQ spectrum, indicating the presence of ionic interactions between TCBQ and electron-donating surface groups (such as carbonyls) on the AC.

Figure 6b presents the XPS O 1s spectra of AC, L-TCBQ, and sc-TCBQ. In both impregnated samples, the most intense O 1s signal originates from C−O groups on the AC support. Importantly, little to no distinct peak from carbonyl (C═O) groups is observed in either L-TCBQ or sc-TCBQ, whereas the bare AC shows a clear C═O component. This absence of a separate quinone carbonyl peak in the impregnated samples does not necessarily mean that the carbonyl groups have disappeared. Instead, it can be explained by two effects: The missing distinct carbonyl feature can be rationalized by attenuation of AC-derived O 1s components by the quinone overlayer and overlap/broadening due to changes in local electrostatic environment and screening at high loading. Accordingly, we treat O 1s as evidence of a changed interfacial environment rather than a unique fingerprint of a specific bonding motif.

Figure 6c shows the XPS C 1s spectra of the activated carbon (AC) and the impregnated samples. In all cases, the prominent peak at ∼284−285 eV corresponds to the C−C bonds of the graphitic carbon framework. Both L-TCBQ and sc-TCBQ also exhibit an additional shoulder/peak on the higher BE side, attributable to the carbons of the TCBQ molecules (notably the carbons bonded to chlorine). For both impregnated samples, the C 1s signal corresponding to C−Cl bonds appear at a lower BE

https://doi.org/10.1021/acsami.5c21457
ACS Appl. Mater. Interfaces 2026, 18, 14947−14959

than the same signal in pure TCBQ, indicating that the carbon bound to chlorine is more electron-rich on AC than in pure TCBQ (i.e., the C−Cl bond is polarized further toward carbon), rather than implying reduction of chlorine. Moreover, when the two methods are compared, the C 1s peak associated with C−Cl in sc-TCBQ is shifted to a slightly lower BE than that in L-TCBQ, by approximately 0.2−0.4 eV. Together with the higher-BE shift of Cl 2p in sc-TCBQ, this opposite-direction behavior is consistent with enhanced C−Cl bond polarization and/or modified final-state screening under $scCO_2$ impregnation. Correspondingly, the intensity of the C−Cl component is higher for sc-TCBQ than for L-TCBQ, implying that a larger fraction of TCBQ in the sc-TCBQ experiences this strongly polarized bonding environment. The opposite-direction shifts—Cl 2p to higher BE and C 1s(C−Cl) to slightly lower BE— are consistent with enhanced interfacial polarization and/or altered screening in sc-TCBQ relative to L-TCBQ. In essence, the enhanced $\pi-\pi$ interactions in sc-TCBQ are consistent with a stronger interfacial dipole and enhanced C−Cl bond polarization under $scCO_2$ impregnation. We refrain from assigning an absolute partial charge based solely on XPS; instead, we interpret the opposite-direction shifts as a qualitative signature of modified interfacial polarization and/or screening associated with denser intrapore packing. Such interfacial charge-transfer-induced core-level shifts are well documented in previous studies of organic molecular junctions and organic semiconductor/substrate interfaces.[63,64]

In summary, relative to the liquid-phase method, the $scCO_2$ route yields distinct electronic structural features for the TCBQ/AC system: (i) the C K-edge XANES of TCBQ (carbon 1s→π^* transition) is blue-shifted under $scCO_2$, and (ii) relative to pure TCBQ, organochlorine-related XPS components shift to higher BE upon supporting on AC; within the supported samples, the Cl 2p peak is slightly higher in sc-TCBQ than in L-TCBQ, whereas the C 1s (C−Cl) component is slightly lower in sc-TCBQ than in L-TCBQ (the inorganic Cl^- signal remains essentially unchanged near ∼198−199 eV). After calibration to the sp^2 C−C reference, these spectral shifts consistently indicate enhanced interfacial polarization and modified screening in sc-TCBQ relative to L-TCBQ. Possible contributions include closer quinone−carbon contact and denser confined packing (including quinone−quinone polarization in confinement); therefore, we discuss these shifts as consistent with, but not definitive proof of, specific Cl···O interaction motifs as schematically illustrated in Figure 7. This enhanced interfacial polarization is consistent with the lower apparent charge-transfer resistance observed in the sc-TCBQ electrodes (discussed below).

Figures 6(d) and (e) show the cyclic voltammetry (CV) results for L-TCBQ and sc-TCBQ under varying scan rates. Overall, the sc-TCBQ electrode delivered lower current responses than L-TCBQ (likely due to differences in loading or conductivity); however, it exhibited better kinetic performance. Notably, as shown in Figure S7, the peak potentials in sc-TCBQ shift less with increasing scan rate, indicating a smaller overpotential under the supercritical conditions. At slow scan rates, the voltammograms of L-TCBQ and sc-TCBQ nearly overlap, and their redox peak positions coincide, confirming that TCBQ undergoes the same two-electron redox reactions in both samples (i.e., the impregnation method does not chemically alter the quinone). As the scan rate increases, the two samples diverge: the redox peaks of sc-TCBQ exhibit smaller potential shifts with increasing scan rate compared to those of L-TCBQ. Figure S8 plots the midpoint redox potential (E_{redox}) as a function of the square root of scan rate ($v^{1/2}$) for both samples. At low v, E_{redox} is identical for L- and sc-TCBQ, but with increasing scan rate, E_{redox} for sc-TCBQ decreases more markedly than that for L-TCBQ. This behavior suggests that the strengthened $\pi-\pi$ interactions in sc-TCBQ facilitate faster electron transfer from the AC surface to the quinone. In practical terms, TCBQ in the $scCO_2$-treated electrode can accept electrons at a slightly lower potential (energy) when the system is under high-rate operation, which means less polarization and improved rate capability for the supercritical sample.

EIS measurements further support the kinetic advantages of sc-TCBQ. The Nyquist plots (Figure 6(f)) show a visibly smaller high-frequency semicircular arc for sc-TCBQ than for L-TCBQ, indicating a lower apparent interfacial resistance associated with the charge-transfer process at the electrode−electrolyte interface. The impedance in the mid- to low-frequency region is also lower for sc-TCBQ, suggesting reduced overall polarization during operation. Quantitatively, ZView semicircle (depressed-arc) estimation shows that the width of the high-frequency arc (taken as the apparent charge-transfer resistance, $R_{ct,app}$) is ∼3.2 Ω for sc-TCBQ and ∼3.7 Ω for L-TCBQ. Moreover, the arc is less depressed for sc-TCBQ, with an estimated CPE exponent α of ∼0.77 (vs ∼0.70 for L-TCBQ), indicating a more ideal capacitive response. The extracted semicircle parameters are summarized in Table S3. Overall, sc-TCBQ exhibits lower apparent charge-transfer resistance and reduced polarization compared to L-TCBQ under the tested conditions, supporting the mechanistic picture that $scCO_2$ treatment promotes more coherent packing of redox-active molecules inside micropores, consistent with the improved utilization observed for sc-DCAQ.

These findings support a clear mechanistic picture: supercritical CO_2 impregnation leads to a more coherent and intimate packing of the TCBQ molecules inside the carbon micropores and stronger electronic coupling at the TCBQ/AC interface. Indeed, the SAXS results indicate that supercritical impregnation of TCBQ yields a higher packing density as shown in Table S4. The result is enhanced $\pi-\pi$ stacking interactions and interfacial charge transfer, in line with the markedly lowered $R_{ct,app}$ and the nearly full active-material utilization observed for sc-DCAQ in our previous studies. In summary, the $scCO_2$ route produces TCBQ-based composite electrodes with improved rate capability and reduced interfacial resistance relative to the conventional liquid impregnation method.

DCAQ, which contains a quinone backbone with chlorine substituents, is expected to exhibit improvements in rate capability and interfacial resistance similar to those observed for TCBQ. Its conjugated structure promotes strong $\pi-\pi$ stacking interactions with the AC surface, facilitating electron transfer and lowering the energy barrier for redox reactions. $ScCO_2$ impregnation is anticipated to improve the dispersion of

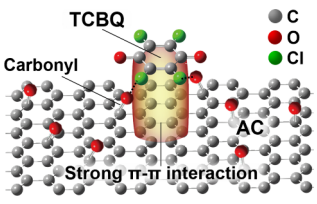


Figure 7. Schematic image of TCBQ adsorption via $scCO_2$ impregnation into AC.

https://doi.org/10.1021/acsami.5c21457
ACS Appl. Mater. Interfaces 2026, 18, 14947−14959

DCAQ, thereby optimizing interfacial contact and charge transport. Moreover, the C−Cl moieties in halogenated quinones may contribute to interfacial electrostatic interactions with oxygen-containing surface groups (e.g., carbonyl functionalities) and thereby influence interfacial polarization. However, distinguishing surface-induced effects from confinement- and packing-related intermolecular polarization would require additional evidence beyond the present XPS data; thus, we frame this point as a plausible contributing factor rather than a definitive assignment.

Extending this concept beyond DCAQ, if other π-electron-rich organic molecules (monomers or molecular catalysts) can be impregnated into porous carbons while maintaining their electrochemical activity, the resulting strengthened $\pi-\pi$ interactions should facilitate faster redox kinetics by improving electronic conductivity and charge transport. For example, conjugated molecular catalysts such as metal phthalocyanines (e.g., iron phthalocyanine) and other redox-active organic monomers (including various quinones or aromatic macrocycles) could particularly benefit from this strategy.[65] Incorporating these π-system molecules into a porous carbon framework is expected to enhance a wide range of electrochemical applications—including organic battery electrodes, fuel-cell catalysts for the oxygen reduction/evolution reactions, and electrochemical sensors—by providing stable molecular anchoring and fast electron pathways that reduce interfacial resistance.[66] This $\pi-\pi$ integration approach thus holds promise for significantly improving the performance of organic electrode materials and molecular catalysts in energy storage and conversion devices.

4. CONCLUSIONS

Ethanol-entrained $scCO_2$ impregnation enabled dense loading of halogenated quinones into high-surface-area microporous carbon with nearly complete utilization of the active material, corresponding to 90% of the micropore-limited theoretical bound. The resulting aqueous all-organic full cell (DCAQ anode/TCBQ cathode) achieved a specific energy of ∼22.3 Wh kg^{-1} at 0.1 A g^{-1}—about 60% higher than that of a liquid-impregnated control—while retaining 54% of its capacity even at 10 A g^{-1} and 95% after 1000 cycles. On a total-electrode-mass basis, these device-level metrics are within the range of legacy aqueous systems and highlight an improved rate response relative to the liquid-impregnated control, while relying exclusively on sustainable, metal-free organic components.

Advanced structural and spectroscopic analyses (SAXS, XAFS, XPS) identified the mechanistic basis of these improvements. $scCO_2$ impregnation produced denser intrapore packing and enhanced $\pi-\pi$ stacking, verified by increased high-q correlation lengths and a blue shift of the C K-edge 1s→π^* resonance. XPS revealed systematic C−Cl/Cl 2p core-level shifts consistent with enhanced interfacial polarization and a modified electronic environment upon $scCO_2$ impregnation (potentially involving changes in screening and confined molecular packing). We avoid assigning a specific partial charge state to chlorine based solely on XPS; instead, these trends support the conclusion that the impregnation route alters the interfacial electronic structure relevant to charge-transfer kinetics.

This work establishes $scCO_2$ impregnation as an effective, solvent-free strategy for interfacial control and near-complete pore utilization. The approach is broadly applicable to other π-conjugated organics—including quinone derivatives and metal phthalocyanines—and could benefit electrochemical systems such as organic batteries, ORR/OER molecular catalysts, and electrochemical sensors. By linking nanoscale molecular organization to device-level performance, this method offers a general and sustainable route toward high-performance, metal-free energy conversion and storage technologies.

■ ASSOCIATED CONTENT

Supporting Information

The Supporting Information is available free of charge at https://pubs.acs.org/doi/10.1021/acsami.5c21457.

Figures S1−S8 (theoretical calculations, SAXS profiles, electrochemical data, redox behavior); Tables S1−S4 (micropore volumes, loading values, capacity utilization, SAXS-derived correlation lengths); detailed experimental methods and calculations for CO_2 sorption, combustion ion chromatography (CIC), SAXS, and electrochemical measurements (PDF)

■ AUTHOR INFORMATION

Corresponding Author

Yuta Nakayasu − *Frontier Research Institute for Interdisciplinary Sciences, Tohoku University, Sendai, Miyagi 980-8578, Japan; Research Center of Supercritical Fluid Technology, Graduate School of Engineering, Tohoku University, Sendai, Miyagi 980-8579, Japan;* orcid.org/0000-0003-2744-099X; Email: nakayasu@tohoku.ac.jp

Authors

Shu Sokabe − *Research Center of Supercritical Fluid Technology, Graduate School of Engineering, Tohoku University, Sendai, Miyagi 980-8579, Japan*

Naoka Nagamura − *Center for Basic Research on Materials, National Institute for Materials Science, Tsukuba, Ibaraki 305-0003, Japan; Graduate School of Advanced Engineering, Tokyo University of Science, Tokyo 125-8585, Japan;* orcid.org/0000-0002-7697-8983

Chie Ooka − *Research Center of Supercritical Fluid Technology, Graduate School of Engineering, Tohoku University, Sendai, Miyagi 980-8579, Japan*

Tomoya Yamada − *Research Center of Supercritical Fluid Technology, Graduate School of Engineering, Tohoku University, Sendai, Miyagi 980-8579, Japan*

Kayoko Kobayashi − *Division of Forest and Biomaterials Science, Graduate School of Agriculture, Kyoto University, Kyoto 606-8502, Japan;* orcid.org/0000-0003-0459-7900

Masaru Watanabe − *Research Center of Supercritical Fluid Technology, Graduate School of Engineering, Tohoku University, Sendai, Miyagi 980-8579, Japan*

Complete contact information is available at: https://pubs.acs.org/10.1021/acsami.5c21457

Notes

The authors declare no competing financial interest.

■ ACKNOWLEDGMENTS

This work was financially supported by the TIA Kakehashi collaborative research program [TK23-022], the Japan Society for the Promotion of Science (JSPS) KAKENHI [grant number 24K01243], the Frontier Research Institute for Interdisciplinary Sciences (FRIS), Tohoku University, and the Tohoku Initiative

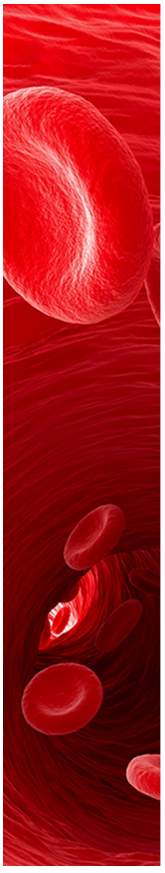
for Fostering Global Researchers for Interdisciplinary Sciences (TI-FRIS) of MEXT's Strategic Professional Development Program for Young Researchers. Generous support from the FRIS CoRE, Tohoku University, which is a shared research environment, is also acknowledged. We thank Prof. Kenichi Ozawa for his support with the XAFS measurements at KEK.

REFERENCES

(1) IEA. *Global EV Outlook 2024*; IEA: Paris, 2024.
(2) Kebede, A. A.; Kalogiannis, T.; Van Mierlo, J.; Berecibar, M. A comprehensive review of stationary energy storage devices for large scale renewable energy sources grid integration. *Renew. Sustain. Energy Rev.* **2022**, *159*, No. 112213.
(3) Sonter, L. J.; Maron, M.; Bull, J. W.; Giljum, S.; Luckeneder, S.; Maus, V.; McDonald-Madden, E.; Northey, S. A.; Sánchez, L. E.; Valenta, R.; Visconti, P.; Werner, T. T.; Watson, J. E. M. How to fuel an energy transition with ecologically responsible mining. *Proc. Natl. Acad. Sci. U. S. A.* **2023**, *120* (35), No. e2307006120.
(4) Surovtseva, D.; Crossin, E.; Pell, R.; Stamford, L. Toward a life cycle inventory for graphite production. *J. Ind. Ecol.* **2022**, *26* (3), 964.
(5) Engels, P.; Cerdas, F.; Dettmer, T.; Frey, C.; Hentschel, J.; Herrmann, C.; Mirfabrikikar, T.; Schueler, M. Life cycle assessment of natural graphite production for lithium-ion battery anodes based on industrial primary data. *J. Clean. Prod.* **2022**, *336*, No. 130474.
(6) Kobayashi, H.; Nakamura, Y.; Nakayama, M.; Kodaki, S.; Matsuo, R.; Honma, I. Metastable cubic structure exceeds capacity limit of antifluorite Li5FeO4 cathode using small polarized oxygen redox. *Adv. Energy Mater.* **2023**, *13* (9), No. 2203441.
(7) Jiao, S.; Wang, J.; Hu, Y.-S.; Yu, X.; Li, H. High-capacity oxide cathode beyond 300 mAh/g. *ACS Energy Lett.* **2023**, *8*, 3025.
(8) Lu, Y.; Zhang, Q.; Li, F.; Chen, J. Emerging Lithiated Organic Cathode Materials for Lithium-ion Full Batteries. *Angew. Chem.* **2023**, *135* (7), No. e202216047.
(9) Zheng, S.; Shi, D.; Sun, T.; Zhang, L.; Zhang, W.; Li, Y.; Guo, Z.; Tao, Z.; Chen, J. Hydrogen Bond Networks Stabilized High-capacity Organic Cathode for Lithium-ion Batteries. *Angew. Chem.* **2023**, *135* (9), No. e202217710.
(10) Hunter, R. D.; Ramírez-Rico, J.; Schnepp, Z. Mater, Iron-catalyzed graphitization for the synthesis of nanostructured graphitic carbons. *J. Chem. A Mater, Energy Sustain.* **2022**, *10*, 4489.
(11) Nakayasu, Y.; Goto, Y.; Katsuyama, Y.; Itoh, T.; Watanabe, M. Highly crystalline graphite-like carbon from wood via low-temperature catalytic graphitization. *Carbon Trends* **2022**, *8*, No. 100190.
(12) Frankenstein, L.; Glomb, P.; Ramirez-Rico, J.; Winter, M.; Placke, T.; Gomez-Martin, A. Revealing the impact of different iron-based precursors on the 'catalytic' graphitization for synthesis of anode materials for lithium ion batteries. *ChemElectroChem* **2023**, *10*, No. e202201073.
(13) Li, Y.; Song, S.; Kim, H.; Nomoto, K.; Kim, H.; Sun, X.; Hori, S.; Suzuki, K.; Matsui, N.; Hirayama, M.; Mizoguchi, T.; Saito, T.; Kamiyama, T.; Kanno, R. A lithium superionic conductor for millimeter-thick battery electrode. *Science* **2023**, *381* (6653), 50.
(14) Dong, D.; Zhao, C.-X.; Zhang, X.; Wang, C. From salt in water, water in salt to beyond. *Adv. Mater.* **2025**, *37*, No. e2418700.
(15) Lee, B.; Seo, H. R.; Lee, H. R.; Yoon, C. S.; Kim, J. H.; Chung, K. Y.; Cho, B. W.; Oh, S. H. Critical role of pH evolution of electrolyte in the reaction mechanism for rechargeable zinc batteries. *ChemSusChem* **2016**, *9* (20), 2948.
(16) Qi, C.; Ye, L.; Ma, X.; Yang, D.; Hong, J. Life cycle assessment of the hydrometallurgical zinc production chain in China. *J. Clean. Prod.* **2017**, *156*, 451.
(17) Qin, T.; Xu, Z.; Wang, Z.; Peng, S.; He, D. 2.5 V salt-in-water supercapacitors based on alkali type double salt/carbon composite anode. *J. Mater. Chem. A* **2019**, *7*, 26011−26019.
(18) Hughson, F. R.; Borah, R.; Nann, T. A 2.7 V aqueous supercapacitor using a microemulsion electrolyte. *Batteries & Amp; Supercaps* **2021**, *4* (7), 1122.
(19) Salisu, A.; Hughson, F.; Borah, R.; Chen, X.; Johns, A.; Griesser, A.; Andersson, G. G.; Nann, T.; Goreham, R. V. Graphene-based supercapacitor using microemulsion electrolyte. *Batter. Supercaps* **2025**, *8*, No. e202400305.
(20) Hong, Y.; Jia, K.; Zhang, Y.; Li, Z.; Jia, J.; Chen, J.; Liang, Q.; Sun, H.; Gao, Q.; Zhou, D.; Li, R.; Dong, X.; Fan, X.; He, S. Energetic and durable all-polymer aqueous battery for sustainable, flexible power. *Nat. Commun.* **2024**, *15* (1), 9539.
(21) Wang, Q.; O'Carroll, T.; Shi, F.; Huang, Y.; Chen, G.; Yang, X.; Nevar, A.; Dudko, N.; Tarasenko, N.; Xie, J.; Shi, L.; Wu, G.; Zhang, D. Designing Organic Material Electrodes for Lithium-Ion Batteries: Progress, Challenges, and Perspectives. *Electrochem, Energy, R.* **2024**, *7*, 15.
(22) Haba, N.; Katsuyama, Y.; Kido, A.; Morimoto, K.; Nakayasu, Y. Direct powder adhesion method of quinone-based aqueous supercapacitor for roll-to-roll process. *Batter. Supercaps* **2025**, *8*, No. e202400721.
(23) Zhong, L.; Liu, C.; Zhang, Y.; Li, J.; Yang, F.; Zhang, Z.; Yu, D. Engineering π-electron Bridge Enables Low-potential 2D Redox Polymer Anodes for High-voltage Aqueous All-organic Batteries. *Angew. Chem.* **2025**, *137*, No. e202413971.
(24) Yu, Z.; Wang, Y.; Luo, Z. Review on redox-active organic compounds for all-organic batteries. *Ind. Eng. Chem. Res.* **2024**, *63* (22), 9619.
(25) Tomai, T.; Mitani, S.; Komatsu, D.; Kawaguchi, Y.; Honma, I. Metal-free aqueous redox capacitor via proton rocking-chair system in an organic-based couple. *Sci. Rep.* **2014**, *4*, 3591.
(26) Otowa, T.; Tanibata, R.; Itoh, M. Production and adsorption characteristics of MAXSORB: High-surface-area active carbon. *Gas Sep. Purif.* **1993**, *7* (4), 241.
(27) Katsuyama, Y.; Nakayasu, Y.; Oizumi, K.; Fujihara, Y.; Kobayashi, H.; Honma, I. Quinone-based redox supercapacitor using highly conductive hard carbon derived from oak wood. *Adv. Sustain. Syst.* **2019**, *3* (11), No. 1900083.
(28) Katsuyama, Y.; Takehi, T.; Sokabe, S.; Tanaka, M.; Ishizawa, M.; Abe, H.; Watanabe, M.; Honma, I.; Nakayasu, Y. Series module of quinone-based organic supercapacitor (> 6 V) with practical cell structure. *Sci. Rep.* **2022**, *12* (1), 3915.
(29) Itoi, H.; Matsuura, M.; Usami, T.; Nagai, Y.; Iwata, H.; Ohzawa, Y. High utilization efficiency of tetramethylbenzoquinone hybridized in the pores of activated carbon for high-performance electrochemical capacitor electrodes. *Carbon Rep.* **2023**, *2* (3), 155.
(30) Itoi, H.; Matsuura, M.; Tanabe, Y.; Kondo, S.; Usami, T.; Ohzawa, Y. High utilization efficiencies of alkylbenzokynones hybridized inside the pores of activated carbon for electrochemical capacitor electrodes. *RSC Adv.* **2023**, *13* (4), 2587.
(31) Komatsu, D.; Tomai, T.; Honma, I. Enhancement of energy density in organic redox capacitor by improvement of electric conduction network. *J. Power Sources* **2015**, *274*, 412−416.
(32) Nakayama, A.; Mizuno, J.; Ohtani, Y.; Shimada, T.; Takagi, S. Elucidation of the Adsorption Distribution of Cationic Porphyrin on the Inorganic Surface by Energy Transfer as a Molecular Ruler. *J. Phys. Chem. C* **2018**, *122*, 4365−4371.
(33) Mirle, C.; Medabalmi, V.; Ramanujam, K. Electrode and Conductive Additive Compatibility Yielding Excellent Rate Capability and Long Cycle Life for Sustainable Organic Aqueous Zn-Ion Batteries. *ACS Appl. Energy Mater.* **2021**, *4* (2), 1218−1227.
(34) Wang, W.; Balland, V.; Branca, M.; Limoges, B. Better Understanding the Role of a Water-in-Salt Electrolyte for Designing a Stable, High-Performance Zinc-Organic Battery. *Chem. Mater.* **2025**, *37* (20), 8364−8382.
(35) Broadbent, P. J.; Carr, C. M.; Lewis, D. M.; Rigout, M. L.; Siewers, E. J.; Shojai Kaveh, N. Supercritical carbon dioxide (SC-CO_2) dyeing of cellulose acetate: An opportunity for a "greener" circular textile economy. *Coloration Technology* **2023**, *139* (4), 475−488.
(36) Nozari, B.; Kander, R. Supercritical CO_2 Technology for Biomass Extraction: Review. *Industrial Crops & Products* **2025**, *233*, No. 121348.
(37) Ushiki, I.; Ota, M.; Sato, Y.; Inomata, H. Measurements and Dubinin−Astakhov correlation of adsorption equilibria of toluene,

https://doi.org/10.1021/acsami.5c21457
ACS Appl. Mater. Interfaces 2026, 18, 14947−14959

acetone, n-hexane, n-decane and methanol solutes in supercritical carbon dioxide on activated carbon at temperature from 313 to 353 K and at pressure from 4.2 to 15.0 MPa. *Fluid Phase Equilib.* **2013**, *344*, 101.
(38) Ushiki, I.; Tahara, Y. Equilibrium adsorption of diethyl ketone on activated carbon in a supercritical CO2 environment: Measurements and thermodynamic modeling. *J. CO2 Util.* **2024**, *84*, No. 102857.
(39) Weidner, E. Impregnation via supercritical CO_2 – What we know and what we need to know. *J. Supercrit. Fluids* **2018**, *134*, 220–227.
(40) Fang, R.; Liang, C.; Xia, Y.; Xiao, Z.; Huang, H.; Gan, Y.; Zhang, J.; Tao, X.; Zhang, W. Supercritical CO_2 mediated incorporation of sulfur into carbon matrix as cathode materials towards high-performance lithium–sulfur batteries. *J. Mater. Chem. A* **2018**, *6*, 212–222.
(41) Zhao, J.; Zhang, L.; Li, X.; Tao, X.; Zhu, W.; Ye, X. Supercritical CO_2 assisted fabrication of activated carbon–sulfur composite for improved lithium–sulfur batteries. *J. Alloys Compd.* **2017**, *708*, 264–269.
(42) Xia, Y.; Zhong, H.; Fang, R.; Liang, C.; Xiao, Z.; Huang, H.; Gan, Y.; Zhang, J.; Tao, X.; Zhang, W. Biomass derived $Ni(OH)_2$@porous carbon/sulfur composites synthesized by a novel sulfur impregnation strategy based on supercritical CO_2 technology for advanced Li–S batteries. *J. Power Sources* **2018**, *378*, 73–80.
(43) Shankar, L. S.; Zalka, D.; Szabo, T.; Szekely, E.; Korosi, M.; Paszti, Z.; Balazsi, K.; Illes, L.; Czigany, Z.; Kun, R. Supercritical carbon dioxide assisted synthesis of ultra-stable sulfur/carbon composite cathodes for Li–S batteries. *Mater. Today Chem.* **2022**, *26*, No. 101240.
(44) Blackburn, J. M.; Long, D. P.; Cabanas, A.; Watkins, J. J. Deposition of conformal copper and nickel films from supercritical carbon dioxide. *Science* **2001**, *294* (5540), 141.
(45) Kondoh, E.; Kato, H. Characteristics of copper deposition in a supercritical CO2 fluid. *Microelectron. Eng.* **2002**, *64* (1–4), 495.
(46) Tomai, T.; Yasui, Y.; Watanabe, S.; Nakayasu, Y.; Sang, L.; Sumiya, M.; Momose, T.; Honma, I. Fabrication of three-dimensional CuInS 2 solar-cell structure via supercritical fluid processing. *J. Supercrit. Fluids* **2017**, *120*, 448.
(47) Garlapati, C.; Madras, G. Solubilities of dodecanoic and tetradecanoic acids in supercritical CO_2 with and without entrainers. *J. Chem. Eng. Data* **2008**, *53* (11), 2637.
(48) Díez-Municio, M.; Montilla, A.; Herrero, M.; Olano, A.; Ibáñez, E. Supercritical CO2 impregnation of lactulose on chitosan: A comparison between scaffolds and microspheres form. *J. Supercrit. Fluids* **2011**, *57* (1), 73.
(49) Shimizu, S.; Abbott, S. How entrainers enhance solubility in supercritical carbon dioxide. *J. Phys. Chem. B* **2016**, *120* (15), 3713.
(50) Nakayasu, Y.; Sokabe, S.; Hiraga, Y.; Watanabe, M. A high-capacity, high-power organic electrode via supercritical CO2 impregnation into activated carbon micropores. *Chem. Commun. (Camb)* **2023**, *59* (21), 3079.
(51) Li, L.; Ma, Z.; Li, Y. Accurate Determination of Optimal Sulfur Content in Mesoporous Carbon Hosts for High-Capacity Stable Lithium-Sulfur Batteries. *Carbon* **2022**, *197*, 200.
(52) Usuki, S.; Uchida, S.; Matsui, Y.; Yamagata, M.; Hinago, H.; Ishikawa, M. Preparation of Micropore-rich High Surface Area Activated Carbon from N-doped Carbon Precursor and its Application to Positive Electrode in Lithium-sulfur Battery. *Electrochemistry* **2017**, *85* (10), 650–655.
(53) Beaucage, G. Approximations Leading to a Unified Exponential/Power-Law Approach to Small-Angle Scattering. *J. Appl. Crystallogr.* **1995**, *28* (6), 717–728.
(54) Beaucage, G. Small-Angle Scattering from Polymeric Mass Fractals of Arbitrary Mass-Fractal Dimension. *J. Appl. Crystallogr.* **1996**, *29* (2), 134–146.
(55) Liu, Y.; Paskevicius, M.; Sofianos, M. V.; Parkinson, G.; Wang, S.; Li, C. Z. A SAXS study of the pore structure evolution in biochar during gasification in H_2O, CO_2 and H_2O/CO_2. *Fuel* **2021**, *292*, No. 120384.
(56) Alwi, R. S.; Tanaka, T.; Tamura, K. Measurement and correlation of solubility of anthraquinone dyestuffs in supercritical carbon dioxide. *J. Chem. Thermodyn.* **2014**, *74*, 119.
(57) Prehal, C.; Weingarth, D.; Perre, E.; Lechner, R. T.; Amenitsch, H.; Paris, O.; Presser, V. Tracking the structural arrangement of ions in carbon supercapacitor nanopores using in situ small-angle X-ray scattering. *Energy Environ. Sci.* **2015**, *8*, 1725–1735.
(58) Debye, P.; Anderson, H. R.; Brumberger, H. Scattering by an Inhomogeneous Solid. II. The Correlation Function and Its Application. *J. Appl. Phys.* **1957**, *28* (6), 679–683.
(59) Härk, E.; Ballauff, M. Carbonaceous Materials Investigated by Small-Angle X-ray and Neutron Scattering. *C* **2020**, *6* (4), 82.
(60) Hirose, T.; Keck, D.; Izumi, Y.; Bamba, T. Comparison of retention behavior between supercritical fluid chromatography and normal-phase high-performance liquid chromatography with various stationary phases. *Molecules* **2019**, *24* (13), 2425.
(61) Ge, J.; Yi, X.; Fan, L.; Lu, B. An all-organic aqueous potassium dual-ion battery. *J. Energy Chem.* **2021**, *57*, 28.
(62) Ng, K. T.; Hercules, D. M. Studies of chloranil-donor adducts by x-ray photoelectron spectroscopy (ESCA). *J. Am. Chem. Soc.* **1975**, *97* (15), 4168.
(63) Tan, K. L.; Tan, B. T. G.; Kang, E. T.; Neoh, K. G. Study of charge-transfer interactions in polyvinylpyridine-halobenzoquinone complexes by x-ray photoelectron spectroscopy. *J. Chem. Phys.* **1989**, *66* (12), 5868–5871.
(64) Nagamura, N.; Fukidome, H.; Nagashio, K.; Horiba, K.; Ide, T.; Funakubo, K.; Tashima, K.; Toriumi, A.; Suemitsu, M.; Horn, K.; Oshima, M. Influence of interface dipole layers on the performance of graphene field-effect transistors. *Carbon* **2019**, *152*, 680–687.
(65) Orellana, W.; Loyola, C. Z.; Marco, J. F.; Tasca, F. Evidence of carbon-supported porphyrins pyrolyzed for the oxygen reduction reaction keeping integrity. *Sci. Rep.* **2022**, *12*, 8072.
(66) Liu, Y.; Ye, H.-Z.; Diederichsen, K. M.; Van Voorhis, T.; Hatton, T. A. Electrochemically mediated carbon dioxide separation with quinone chemistry in salt-concentrated aqueous media. *Nat. Commun.* **2020**, *11* (1), 2278.


CAS BIOFINDER DISCOVERY PLATFORM™
CAS BIOFINDER HELPS YOU FIND YOUR NEXT BREAKTHROUGH FASTER
Navigate pathways, targets, and diseases with precision
Explore CAS BioFinder
CAS
A division of the American Chemical Society

https://doi.org/10.1021/acsami.5c21457
ACS Appl. Mater. Interfaces 2026, 18, 14947–14959